Chinese Journal of Chemical Engineering 87 (2025) 369–380

Contents lists available at ScienceDirect

Chinese Journal of Chemical Engineering

journal homepage: www.elsevier.com/locate/CJChE

Full Length Article

Effective removal of fluoride from wastewater by magnesium oxide-loaded aeolian sand with high loading ratio

Chenxin Ding [1, 2], Zhen Jin [1, 2, *], Qianxi Li [1, 2], Shuhao Zhou [1, 2], Yuru Sun [1, 2]

[1] School of Materials and Chemical Engineering, Anhui Jianzhu University, Hefei 230601, China
[2] Anhui Advanced Building Materials Engineering Laboratory, Anhui Jianzhu University, Hefei 230601, China

ARTICLE INFO

Article history:
Received 27 December 2024
Received in revised form
30 April 2025
Accepted 7 May 2025
Available online 22 July 2025

Keywords:
Fluoride removal
Magnesium oxide
Aeolian sand
Adsorption

ABSTRACT

In this study, a facile and effective hydrothermal approach was developed to synthesize magnesium oxide loaded aeolian sand (MOAS) with a high loading ratio as an environmentally friendly adsorbent for effective removal of fluoride from wastewater. The analysis of material morphology and structure revealed that the MOAS has a stacked structure and the magnesium oxide is successfully loaded on the surface of aeolian sand with high loading ratio (230%). The adsorption kinetics demonstrated that the adsorption of fluoride by MOAS followed the pseudo-second-order model. The adsorption isotherm conformed to the Redlich-Peterson model with a saturated adsorption capacity of 153.11 $mg \cdot g^{-1}$. MOAS exhibited excellent defluorination performance over a wide pH range and in the presence of competitive anion, respectively. The density functional theory (DFT) theoretical calculations verify that the MOAS has strong affinity for fluoride. The adsorption mechanism was investigated through FTIR and XPS, revealing that hydroxyl exchange and coordination on the surface were responsible for the defluorination of MOAS. Finally, desorption, regeneration, adsorption column experiments and actual wastewater experiment further confirmed the practical potential of MOAS for defluorination applications.

1. Introduction

In recent years, China's photovoltaic industry has developed rapidly. Photovoltaic modules are widely used in various industries, such as agriculture, industry, business and household. These photovoltaic modules provide great convenience for people's lives. However, a large amount of high fluorine wastewater will be produced in the production process of photovoltaic modules. These wastewaters can cause serious pollution to the environment and ecosystems, resulting in fluoride concentrations in drinking water exceeding acceptable standards. Drinking water with high fluoride concentrations for a long time can lead to a range of health issues within the human body, including dental fluorosis, skeletal fluorosis, neurotoxicity, and toxicity to the liver and kidneys [1–3]. Therefore, the defluorination of high fluoride drinking water is of great significance.

Currently, numerous methods are available for fluoride removal, including adsorption [4], precipitation [5], precipitation [6], and electrodialysis [7]. Among these methods, adsorption is extensively employed due to its advantages, including operational simplicity and cost-effectiveness. During the past few years, many fluoride removal adsorbents have been developed, such as activated charcoal [8], graphene [9], biochar [10], zeolite [11], clay [12], and pumice [13]. However, carbon-based compounds and natural minerals necessitate multiple regeneration cycles due to lower saturated adsorption capacity, thereby increasing the overall cost of the adsorbent. In contrast, metal oxides have high adsorption capacity for fluoride. As a metal oxide, magnesium oxide has many advantages, such as high adsorption capacity, strong affinity, large specific surface area, non-toxicity, high porosity, low price, and easy access. Therefore, magnesium oxide is very suitable as an adsorbent for fluoride removal. Various magnesium oxide-based adsorbents have been prepared in previous studies, such as porous MgO nanoplates [14], MgO nanofibers [15], and MgO microspheres [16]. The adsorption capacities of these adsorbents are all above 100 $mg \cdot g^{-1}$. However, the high surface energy of magnesium oxide is prone to aggregation and agglomeration [17,18], which limits the reusability of adsorbents and adversely affects its economic viability. The aforementioned challenges can be addressed through the preparation of nano-composite materials by judiciously selecting appropriate substrate materials and leveraging the inherent advantages of nanomaterials. Recently,

* Corresponding author.
E-mail address: ftbjin@hotmail.com (Z. Jin).

https://doi.org/10.1016/j.cjche.2025.05.030

magnesium oxide composites have prepared, such as magnesium oxide entrapped polypyrrole hybrid [19], and magnesia/chitosan composite [20]. These composites remarkably enhance the adsorption capacity towards fluoride and solve the problem of agglomeration, but the preparation of substrate materials is relatively complex, and the loading capacity of the active material is comparatively low. Therefore, it is particularly important to select the appropriate substrate material.

Aeolian sand is a widely prevalent natural material. In northern China, the intense weathering and denudation of rock contribute to the accumulation of aeolian sand reserves. Therefore, aeolian sand can be used as a kind of exploitable green resource, which has the advantages of low development cost and environmental protection. Meanwhile, the surface morphology of aeolian sand is distinct from that of other substrate materials, which is characterized by a smooth texture with angular features, and the particle size of aeolian sand predominantly ranges from 0.075 to 0.3 mm. It can be suitable for the filler of the adsorption column. Furthermore, the primary constituent of aeolian sand is SiO_2, resulting in a surface that is abundant in hydroxyl groups. Based on these characteristics, metal ions exhibit a greater propensity to adhere to the surface of aeolian sand, thereby facilitating the growth of metal nanoparticles. In prior research, aeolian sand has predominantly been utilized as a construction material. Nonetheless, there is a paucity of investigation within the adsorption domain, and utilizing aeolian sand as a substrate material significantly reduces the preparation costs associated with the adsorbent. Therefore, aeolian sand can be used as a potential adsorption substrate material and consider the magnesium oxide loaded on the aeolian sand substrates. This innovative methodology capitalizes on the synergistic combination of MgO's well-documented fluoride adsorption capacity and the underutilized potential of aeolian sand as a porous support matrix. Notably, the utilization of aeolian sand as an substrate represents a novel application in water treatment technologies, with limited prior art documented in scientific literature.

The proposed synthesis strategy is magnesium oxide loaded aeolian sand, effectively addressing the common agglomeration and inhomogeneity issues associated with direct magnesium oxide granulation. In addition, the multi-step loading method is used to increase the MgO loading ratio, so that the synthesized material particles are more uniform. The resulting magnesium oxide functionalized aeolian sand composite demonstrates significant potential as an advanced fluoride removal material.

In this work, magnesium oxide loaded aeolian sand (MOAS) with a high loading ratio was successfully prepare by hydrothermal synthesis method for effective removal of fluoride from wastewater. Under the optimal synthesis conditions, the loading ratio of magnesium oxide can reach 230%. The adsorption performance of MOAS was investigated through the experiments on adsorption kinetics, adsorption isotherms, the pH effect, and competitive anion interference. The FTIR and XPS analysis illustrated that the adsorption mechanism could be attributed to coordination exchange and surface hydroxyl exchange. The DFT theoretical calculation proved that MOAS had selectivity to fluoride. Desorption, regeneration, column experiments and actual wastewater experiment further substantiated the practical applicability of MOAS in defluorination process.

2. Materials and Methods

2.1. Experimental materials

Aeolian sand was gathered from Inner Mongolia, China. Magnesium sulfate heptahydrate ($MgSO_4{\cdot}7H_2O$), glacial acetic acid (CH_3COOH), and polyethylene glycol ($HO(CH_2CH_2O)_nH$) were purchased from Shanghai Macklin Biochemical Technology Co., Ltd. Urea ($CO(NH_2)_2$), trisodium citrate dihydrate ($C_6H_5Na_3O_7{\cdot}2H_2O$), and the supplier of sodium fluoride (NaF) was Sinopharm Chemical Reagent Co., Ltd. All the pharmaceuticals are of analytical purity.

2.2. Synthesis of MOAS

Firstly, the aeolian sand was rinsed with deionized water to remove surface impurities, and then dried in an oven at 60 °C for 12 h. The dried aeolian sand was soaked in 1 $mol{\cdot}L^{-1}$ NaOH solution for 12 h and rinse with deionized water and subsequently dry in an oven at 60 °C for 12 h. Secondly, the MOAS synthesis process is shown in Fig. S1, Supplementray Material. After adding $MgSO_4{\cdot}7H_2O$, urea, and polyethylene glycol to 40 ml of deionized water, the mixture was allowed to dissolve for 10 min. The aforementioned solution, along with 1 g of aeolian sand, was transferred to a 250 ml conical flask and subjected to heating in an oven at 100 °C for 12 h. The precipitate was collected and washed with deionized water, and then dried in an oven at 60 °C for 12 h. The dosing step was repeated to obtain magnesium oxide loaded aeolian sand with different loading times (MOAS-*X*, *X* represents the loading time). As shown in Fig. S2, XRD results of MOAS at different annealing temperatures showed that the precursor was transformed into MOAS after calcination at 500 °C for 4 h, and there is no excess precursor residue. The loading ratio of magnesium oxide (L_{MO}, %) was evaluated according to the following equation:

$$L_{MO} = \frac{m_1 - m_2}{m_2} \tag{1}$$

where m_1 is the mass of MOAS (g) and m_2 is the mass of MOAS after dissolving the magnesium oxide by 1 $mol{\cdot}L^{-1}$ HCl (g).

2.3. Material characterization

Scanning electron microscopy was used to characterize the morphology of MOAS (SEM, JEOL, JSM7500F, Japan) and transmission electron microscopy (TEM, JEOL, JEM-F20, Japan). Using X-ray diffractometer (XRD, Rigaku, Smartlab, Japan), the crystal structure of MOAS was described. The XRD scanning was conducted over a range of 5° to 80° with a scanning rate of 40(°)·min^{-1}. A fully automatic specific surface area and aperture distribution analyzer (Quantachrome, Autosorb-IQ, USA) was employed to conduct the BET analysis. Using a synchronous thermal analyzer (Netzsch, STA409PC, Germany), the differential scanning calorimetric (TG-DSC) curves were examined. Thermogravimetric differential scanning calorimetry was performed in N_2 atmosphere at a temperature rise rate of 10 °C·min^{-1}. The zeta potential of MOAS was analyzed by particle size distribution and zeta potentiometer (Malvern, Nano ZSE, UK). The X photoelectron spectrometer (Thermo Fisher, ESCALAB QXi, USA) was used to evaluate the MOAS X-ray photoelectron spectroscopy (XPS). A Fourier infrared spectrometer (Thermo Fisher, Nicolet 6700, USA) was used to evaluate the MOAS Fourier Transform infrared spectrums (FTIR).

2.4. Adsorption experiment

The adsorption kinetics experiments were carried out by adding 200 ml NaF solution and 5 g·L^{-1} MOAS into a 250 ml wide-mouth conical flask without adjusting the pH value. The level of fluoride concentration was 10 mg·L^{-1}. The sampling time was 3, 5, 7, 9, 15, 20, 50, 80, 120, 180, 360, and 720 min, respectively.

The adsorption isotherm experiment was carried out by adding 10 ml NaF solution and 1 g·L^{-1} MOAS into a 15 ml centrifuge tube.

The pH effect and competitive anion interference experiments were carried out by adding 10 ml of NaF solution and 5 g·L^{-1} of MOAS in 15 ml centrifuge tubes. In the experiment, the pH was adjusted from 3 to 13 using NaOH and HCl solution. The influence of competitive anions on the adsorption of fluoride by MOAS was investigated with CO_3^{2-}, HCO_3^-, Cl^-, SO_4^{2-} and PO_4^{3-}. The adsorption column had a volume of 5 ml and was 100 mm in height. The influent fluoride concentration was established at 5 mg·L^{-1}, whereas the space velocity (SV) was modulated to magnitudes of 4 h^{-1} and 8 h^{-1}, respectively. The wastewater experiment was carried out by adding 200 ml of actual wastewater and 5 g·L^{-1} of MOAS into 250 ml wide-mouth conical flask.

The test solution was extracted with a 5 ml disposable syringe and filtered through a 0.45 μm filter. Fluoride concentration was determined by the ion selective electrode method.

2.5. DFT analysis

All the first-principles calculations were performed in Materials Studio software. All model structures were further optimized by the CASTEP software package. In this study, the exchange-related electron interaction energy was simulated by means of the generalized gradient approximation (GGA) method with Perdew-Burke-Ernzerhof (PBE) functional. An energy convergence tolerance of 2.0 × 10^{-6} eV· atom^{-1} and an energy cutoff of 490 eV were used. In order to calculate the adsorption energy, the strongest diffraction peak of the (200) plane was used as the adsorption surface, and a vacuum layer of 1.5 nm was established to prevent the interaction between the two repeated layers. The adsorption energy (E_{ads}) was calculated according to the following formula:

$$E_{ads} = E_{Total} - E_{MOAS} - E_x \quad (2)$$

where E_{ads} denotes the adsorption energy, E_{Total} represents the total energy of the system after the adsorption of ions by MOAS, E_{MOAS} indicates the energy of the before adsorption of the MOAS, and E_x delegates the energy of a single ion.

3. Results and Discussion

3.1. Materials characterization

The XRD pattern of aeolian sand, precursor, and MOAS were shown in Fig. 1. The results illustrate that the principal component of aeolian sand is SiO_2 (JCPDS 70-3755). After hydrothermal reaction for 12 h, the diffraction peak of the precursor corresponds to $Mg_5(CO_3)_4(OH)_2\cdot(H_2O)_4$ (JCPDS 70-0361). Nonetheless, the diffraction peaks of MOAS after annealing correspond to MgO (JCPDS 89-7746). The parameters of the unit cell are $a = b = c = 4.213$, $\alpha = \beta = \gamma = 90°$. The above results illustrated that the material MOAS is successfully prepared after hydrothermal reaction and heat treatment.

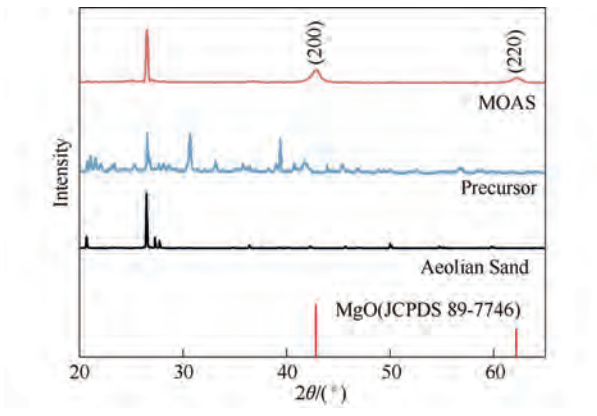

Fig. 1. XRD patterns of aeolian sand, precursor, and MOAS.

As illustrated in Fig. 2(a) at lower magnification, the surfaces of the aeolian sand particles appear relatively smooth and nearly rounded, with distinct corners present at their edges. Obvious shell sheet debris can be observed on the surface of aeolian sand at high magnification, which may be caused by long-term weathering and denudation of rock. Fig. 2(b) shows that the surface morphology of the synthesized MOAS is completely different from that of the aeolian sand. The surface of MOAS becomes rough due to the stacking of magnesium oxide particles. As displayed in Fig. 2(c), MOAS is observed at high magnification. The surface of MOAS is observed to be densely populated with sheet magnesium oxide, exhibiting a disordered stacking structure that creates numerous pores. In Fig. 2(d), it was further observed that the surface of the sheet is rough and stacked with each other, which provides more active sites for adsorption of fluoride by MOAS. As displayed in Fig. S3, the SEM-EDS elemental mapping of MOAS show that MgO is uniformly loaded on the surface of aeolian sand. This further illustrates the successful synthesis of MOAS. As illustrated in Fig. 2(e) and (f), numerous nanopores are generated by MOAS, with the release of CO_2 and H_2O during the annealing process contributing to their formation. Fig. 2(g) displays the HRTEM image of MOAS, revealing a lattice spacing of 0.210 nm that is associated with the (200) crystal plane of MOAS. Moreover, the corresponding selected area electron diffraction (SAED) with the polycrystalline diffraction rings (111), (200), and (220) of MOAS is observed in Fig. 2(h).

The Brunauer-Emmett-Teller (BET) method is employed to conduct a further analysis of the microstructure of MOAS. As illustrated in Fig. 3(a), the N_2 adsorption-desorption curves exhibit IV-type isotherms accompanied by H3-type hysteresis loops, indicating the typical mesoporous characteristic of MOAS. And the pore size distribution of MOAS shows a multi-peak distribution, and the peak of the maximum geometric pore size is at 7.8 nm. The mesoporous structure formed by the stacking of magnesium oxide increased the specific surface area of MOAS, which is calculated to be 27.47 m^2·g^{-1}. The extensive specific surface area furnishes additional active sites for fluoride adsorption by MOAS. Meanwhile, it can be proved that MOAS with high specific surface area is a potential material for fluoride removal.

In order to further elucidate the synthesis of MOAS, TG-DSC analysis is performed on the precursor of MOAS in Fig. 3(b). The synthesis steps can be summarized as follows: Based on Eq. (3), urea dissolves and decomposes pyrolytically to NH_4^+, CO_3^{2-} and OH^-. On account of Eq. (4), the Mg^{2+} ions, which are adsorbed by aeolian sand, react with CO_3^{2-} and OH^- to produce precursors of MOAS. According to Eq. (5), the precursor undergoes annealing, resulting in the release of hydroxyl groups as water vapor and carbonates as carbon dioxide. The MOAS is finally obtained. According to the formula, the theoretical content of MgO should be 42.92%.

$$CO(NH_2)_2 + 2H_2O \rightarrow 2NH_4^+ + CO_3^{2-} + OH^- \quad (3)$$

$$5Mg^{2+} + 2OH^- + 4CO_3^{2-} + 4H_2O \rightarrow Mg_5(CO_3)_4(OH)_2\cdot(H_2O)_4 \quad (4)$$

$$Mg_5(CO_3)_4(OH)_2\cdot(H_2O)_4 \rightarrow 5MgO + 4CO_2 + 5H_2O \quad (5)$$

Fig. 4(a)–(l) shows SEM images of MOAS in different cycles of synthesis. After the first synthesis cycle, a few magnesium oxide sheets grow on the surface of the aeolian sand. With the increase

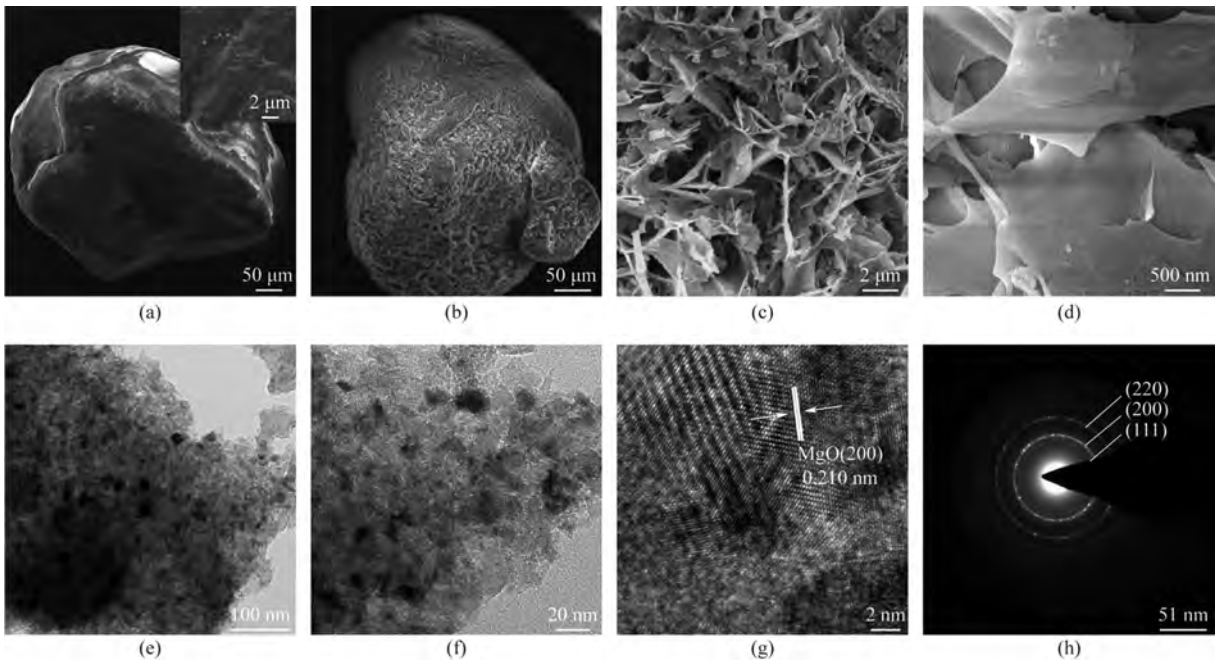

Fig. 2. (a) SEM image of aeolian sand, (b, c and d) SEM images of MOAS at different magnifications, (e and f) the TEM of MOAS, (g) the corresponding HRTEM image, and (h) the corresponding SAED pattern.

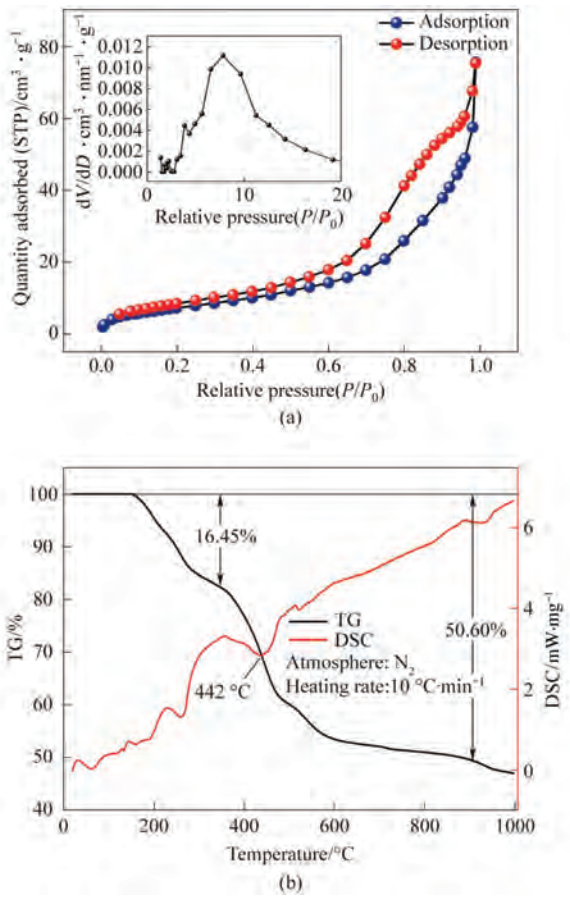

Fig. 3. (a) The Brunauer-Emmett-Teller of MOAS, (b) TG-DSC curves of precursor.

of the cycles of synthesis, magnesium oxide is attracted to the surface of aeolian sand. The coverage area of magnesium oxide on the surface of aeolian sand gradually grows larger, and the magnesium oxide sheet gradually stacks. After five cycles, the surface of the aeolian sand is basically covered by magnesium oxide, forming a large number of sheets stacked structures. This observation is corroborated by Fig. 4(m), which illustrates the color change of aeolian sand as magnesium oxide is progressively encapsulated, resulting in a gradual whitening of the material. The characterization results demonstrate that the sequential loading processes effectively reduce MgO's surface energy, enabling uniform dispersion on aeolian sand surfaces. Through iterative loading cycles, interfacial stress between MgO layers is progressively released, facilitating precise morphology control. Repeated loading further constructs a hierarchical porous structure on MgO surfaces, significantly enhancing active site accessibility and surface reactivity compared to single loading approaches.

As a surfactant, polyethylene glycol employs its long-chain structure to encapsulate the crystals, while hydroxyl groups facilitate the adsorption of free metal ions [21]. This mechanism prevents collisions between particles, improves dispersion, and reduces agglomeration. Polyethylene glycol facilitates a more uniform distribution of magnesium oxide on the surface of aeolian sand. To investigate the relationship between synthesis conditions and the loading ratio of MgO, orthogonal experiments have been designed. The effects of $MgSO_4 \cdot 7H_2O$, polyethylene glycol, and synthesis cycle on the loading ratio of magnesium oxide are studied in Fig. 5. The experimental parameters included $MgSO_4 \cdot 7H_2O$ (2, 4, 6, and 8 g), polyethylene glycol (0, 0.2, 0.4, and 0.6 g), and synthesis cycles ranging from 1 to 5. When the synthesis cycle was 5 times, the dosage of $MgSO_4 \cdot 7H_2O$ was 4 g, and the dosage of polyethylene glycol was 0.6 g, the maximum loading ratio of magnesium oxide was 230%. When the synthesis period exceeds 5 times, the loading ratio gradually tends to be gentle. This may be due to the large

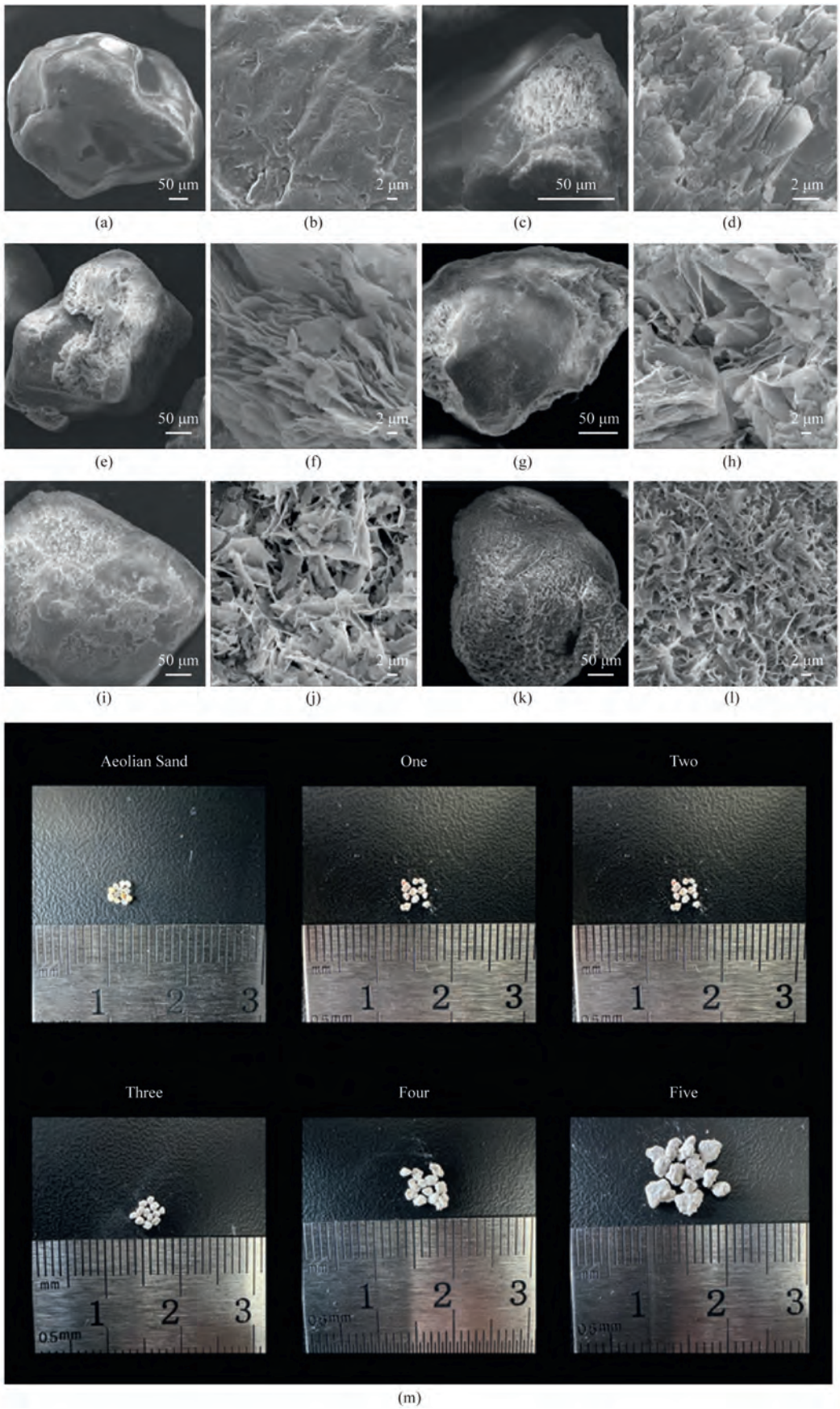

Fig. 4. (a–l) SEM images of MOAS in different cycles of synthesis and (m) Digital images of MOAS in different cycles of synthesis.

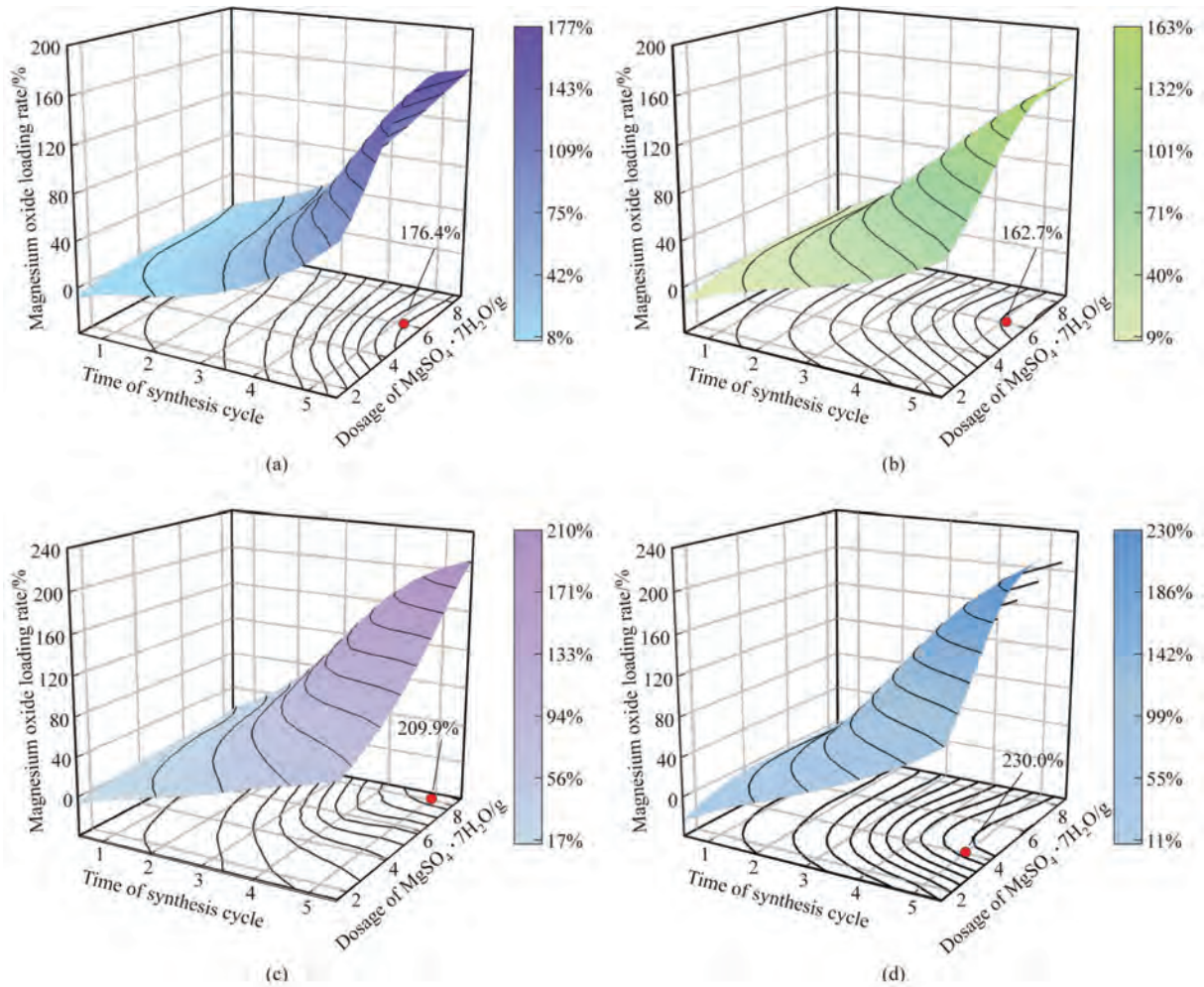

Fig. 5. The effect of synthesis conditions on the loading ratio under different dosages of polyethylene glycol: (a) 0 g, (b) 0.2 g, (c) 0.4 g, and (d) 0.6 g .

amount of magnesium oxide loaded on the surface of aeolian sand, resulting in the accumulation of a large number of particles. Free magnesium oxide is difficult to load on the surface of aeolian sand. As illustrated in Fig. S4(a)–(p), the optimal adsorption capacity of 153.11 mg·g^{-1} for MOAS was achieved under conditions of 4 g $MgSO_4 \cdot 7H_2O$, 0.6 g polyethylene glycol, and 5 synthesis cycles. The adsorption properties were consistent with the loading ratio. This optimized parameter set was consequently adopted as the standardized protocol for all subsequent material syntheses in the performance evaluation experiments.

3.2. Adsorption kinetics

As shown in Fig. 6(a), the adsorption kinetics fitting curves show that the removal efficiency of fluoride has completed more than 70% in 60 min. Table S1 shows that the correlation coefficient (R^2>0.993) of the pseudo-second-order model is highest, which demonstrates that the chemical adsorption procedure dominates in the adsorption of fluoride by MOAS. Meanwhile, K_2 reflects the adsorption rate of MOAS to fluoride. The faster the adsorption rate is, the smaller the K_2 value [22]. The K_2 value of MOAS ($K_2 = 0.142$) is significantly lower than that of granular matrix supported nano magnesium oxide [23] and iron oxides modified available sand [24], indicating that the adsorption rate of fluoride by MOAS has been significantly improved.

3.3. Adsorption isotherms

As shown in Fig. 6(b), the saturated adsorption capacity of MOAS is 153.11 mg·g^{-1}. Table 1 shows the comparison of adsorption properties of MOAS and other adsorbent materials. MOAS keeps ahead in comparison with other defluorination adsorbents. Fig. S5 and Table S2 showed the fit results of four isothermal model. The Redlich-Peterson model of MOAS with different times of synthesis cycles have the highest correlation coefficient: aeolian sand (R^2>0.841), MOAS-1 (R^2>0.991), MOAS-2 (R^2>0.971), MOAS-3 (R^2>0.929), MOAS-4 (R^2>0.968) and MOAS-5 (R^2>0.977), respectively. This demonstrates that the Redlich-Peterson model can describe the adsorption behavior of MOAS with greater accuracy. The magnitude of the K_R value reflects the affinity of the adsorbent for the adsorbate. The results of the fitted parameters indicate that the K_R value increases progressively with an increasing number of modifications, suggesting that MOAS exhibits a strong affinity for fluoride and adsorbs it more readily [25]. Meanwhile, the value of the parameter β_R gradually approaches 0, indicating that the Redlich-Peterson model has a closer alignment with the Freundlich model, thereby suggesting the presence of multilayer adsorption in the adsorption process. According to the model, the adsorption capacity of MOAS exhibits a nonlinear relationship with fluoride concentration, indicating that the adsorption process is constrained by available adsorption sites. Consequently, the adsorption rate will gradually plateau as these sites become saturated.

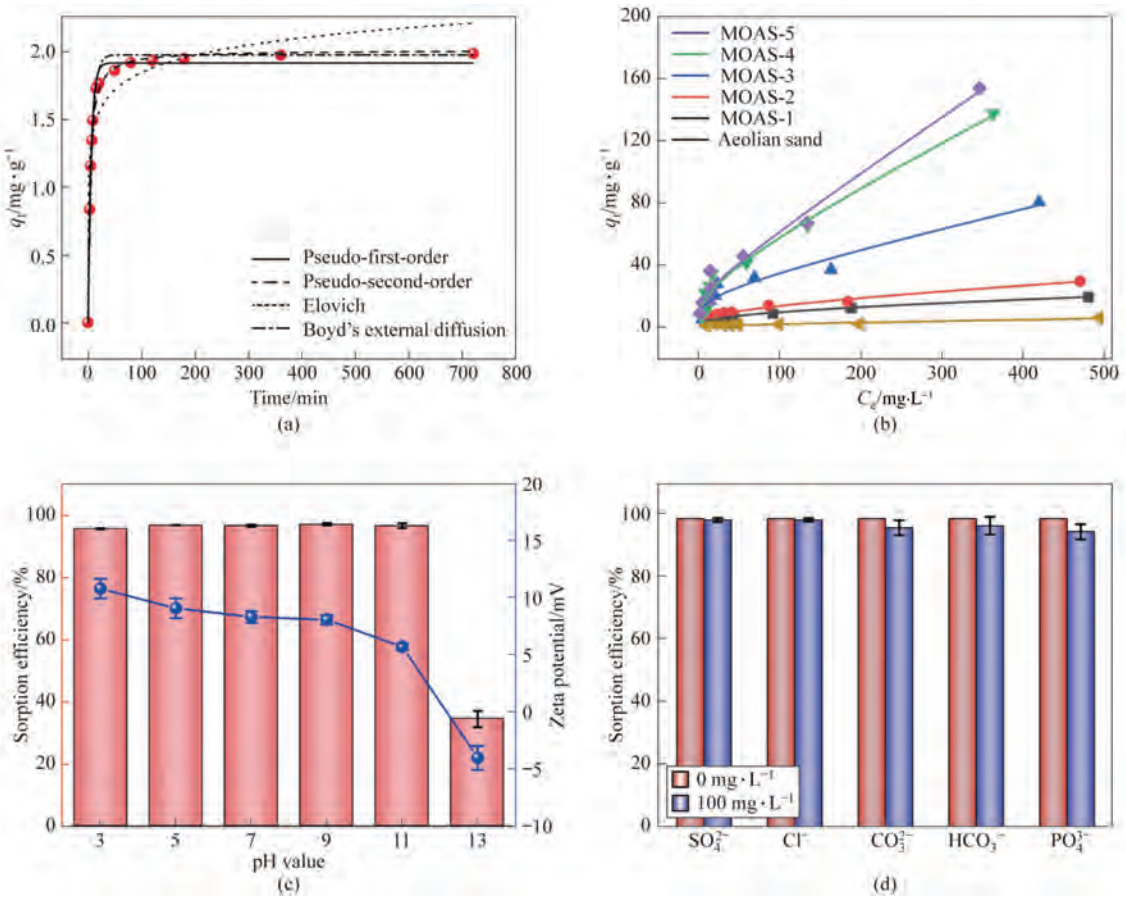

Fig. 6. (a) Adsorption kinetics of MOAS, (b) Redlich–Peterson model fitting for MOAS isothermal adsorption, (c) fluoride removal efficiency and zeta potential values of MOAS at different pH values, and (d) effect of competitive anions on fluoride removal efficiency of MOAS.

3.4. Effect of pH value and competitive anions on defluorination efficiency of MOAS

The pH was changed using HCl and NaOH to examine the MOAS removal effectiveness for fluoride at various pH values. The fluoride concentration is 10 mg·L^{-1} and the adsorbent amount is 5 g·L^{-1}. As shown in Fig. 6(c), MOAS maintains a high removal efficiency of fluoride at pH < 13. However, the removal efficiency decreases significantly at pH = 13. Meanwhile, the research has demonstrated that the efficacy of metallic materials in fluoride removal is ascribed to the amphoteric characteristics of metal surfaces [23]. Therefore, the zeta potential values of MOAS at different pH values were measured to represent the electrically charged nature of the MOAS surface [26]. The pH_{zpc} of MOAS is observed to be 12.3. Nevertheless, reactions that promote fluoride interactions predominantly take place within the pH range below the zero-surface charge, thereby allowing MOAS fluoride removal to exhibit a broad operational pH spectrum. The trends of fluoride removal efficiency and zeta potential value of MOAS at different pH were similar, and the zeta potential value of MOAS decreased rapidly at pH = 13. This suggested that the magnitude of charge carried on the surface of MOAS is the primary cause of the change in fluoride removal efficiency. MOAS is positively charged at pH < pH_{zpc}, and Mg–O on the surface of MOAS is highly protonated [27], which promotes ligand exchange with fluoride. When pH > pH_{zpc}, An abundance of hydroxyl groups in the solution affect the protonation of Mg–O, reducing the formation of protonated product Mg–OH$^+$. The hydroxyl exchange between Mg–OH$^+$ and fluoride is inhibited, and the removal efficiency is significantly reduced.

To assess the adsorption capability of MOAS for fluoride in practical applications, 100 mg·L^{-1} of various anion solutions was introduced into a solution containing 10 mg·L^{-1} fluoride, with the adsorbent concentration maintained at 5 g·L^{-1}. As illustrated in Fig. 6(d), Cl^- and SO_4^{2-} exert minimal influence on adsorption, whereas the effects of HCO_3^-, CO_3^{2-}, and PO_4^{3-} primarily arise from competition among these anions and the sites on the MOAS surface for fluoride adsorption [28]. The influence of these anions on the defluorination efficacy of MOAS follows the order: CO_3^{2-} < HCO_3^- < PO_4^{3-}.

3.5. Mechanism analysis

In order to further illustrate the selectivity of MOAS to fluoride ions. The DFT calculation was used to determine the adsorption energy of MOAS adsorbing fluoride ions. As shown in Fig. 1, XRD analysis shows that MgO calcined at 500 °C has the best crystallinity on the (200) plane and the strongest diffraction peak, which is more stable than other crystal planes and more suitable for DFT calculation. Secondly, studies have shown that MgO with (200) crystal plane has exposed oxygen active sites and mesoporous networks, increasing the surface area of the adsorbent [29]. Comparative analysis of (200) facet versus other crystallographic orientations. The (110) crystal plane exhibits high surface energy prone to reconstruction [30], with its zigzag atomic arrangement creating complex adsorption site configurations that necessitate larger supercell with challenging convergence [31]. Furthermore, the polar surface of the (111) surfaces exhibit strong dipole moments requiring charge compensation mechanisms (complicated

Table 1
Comparison of different fluoride removal adsorbents.

Adsorbents	Sorption capacity/mg·g^{-1}	pH	Ref.
$CeCO_3OH$	45	7	[41]
Ce–La oxides	662.25	4	[42]
La–Zr composite	88.5	3	[43]
Mg–Fe binary metal	249	3	[44]
MgO porous nanoplates modified pumice	37.9	2–10	[45]
CS–ZFA	37.49	6	[46]
Magnesium oxide nanoparticles	372.65	7	[35]
MgO microspheres	115.5	7	[16]
MgO nanofibers	294	6	[15]
Alumina hollow spheres	16.77	7	[47]
Iron oxide	60.8	3.5–10.3	[48]
MOAS	**153.11**	**7**	**This work**

model construction), coupled with experimental instability and poor theoretical-experimental consistency [32,33]. Therefore, the strongest diffraction peak of the (200) surface was used as the adsorption surface, and a 1.5 nm vacuum layer was established for DFT calculation. The adsorption strength is reflected in the absolute value of the adsorption energy. The more stable the adsorption structure, the higher the value. Fig. 7's computation results indicated the E_{ads} of the F^-, Cl^-, PO_4^{3-}, SO_4^{2-}, HCO_3^- and CO_3^{2-} are −14.4 eV, −4.9 eV, −13.7 eV, −13.4 eV, −9.6 eV and −8.9 eV, respectively. Therefore, MOAS has the most stable adsorption structure of F^-.

Fig. 8 shows FTIR spectra of aeolian sand and MOAS before and after adsorption. The matching stretching vibration to OH^- was observed at 3448 cm^{-1} in aeolian sand, pre-adsorption MOAS, and after-adsorption MOAS. This phenomenon can be ascribed to the ability of MOAS to absorb moisture in the atmosphere [34].

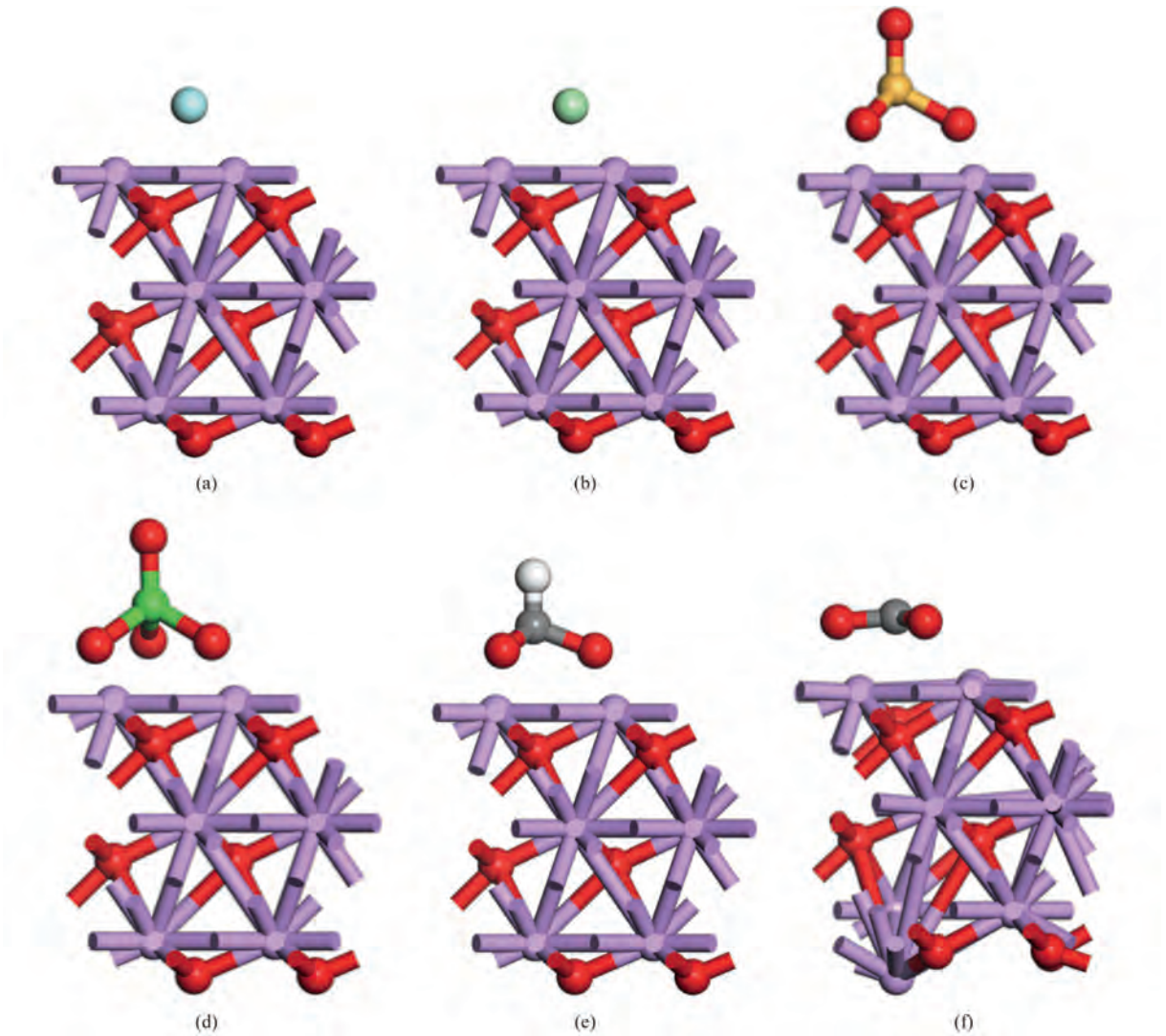

Fig. 7. The adsorption energy of MOAS after adsorption (a) adsorption of F^-, (b) adsorption of Cl^-, (c) adsorption of PO_4^{3-}, (d) adsorption of SO_4^{2-}, (e) adsorption of HCO_3^- and (f) adsorption of CO_3^{2-}.

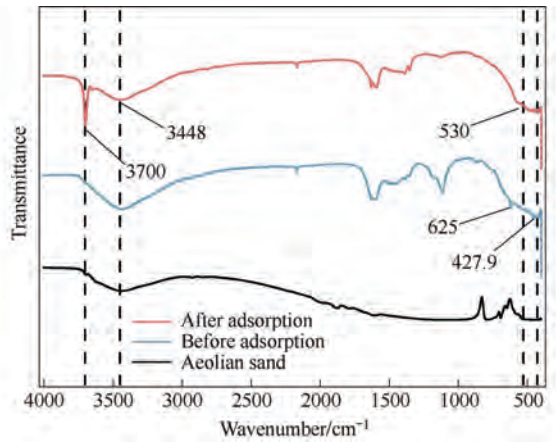

Fig. 8. FTIR spectra of aeolian sand and MOAS before and after adsorption.

However, the peak strength was significantly weakened after adsorption, indicating that fluorine ions replaced OH^- during the adsorption of fluoride. After adsorption, the absorption peak at 3700 cm^{-1} becomes stronger, which can be credited to the reaction of MOAS with water to produce $Mg(OH)_2$ [14]. The absorption peak at 625 cm^{-1} can be attributed to Si—O stretching vibration of aeolian sand [27]. The stretching vibration in proportion to Mg—O was obviously observed at 427.9 cm^{-1} before adsorption [21,35]. In the course of the adsorption process, however, the peak at 427.9 cm^{-1} diminishes, while a new peak emerges at 530 cm^{-1}, which can be attributed to Mg—F stretching vibrations [14,16].

Fig. 9(a) presents the XPS spectra of MOAS before and after fluoride adsorption. It can be seen that a new peak of F 1s appears at 684.9 eV after adsorption, and the emergence of the new peak can be more visibly observed through the narrow spectrum of F1s photoelectrons in Fig. 9(b) [36]. Before adsorption of fluoride, the peak at 49.96 eV is generated by the binding of Mg—O atoms, while the peak at 49.24 eV is caused by the binding of Mg—OH [36,37] (Fig. 9c). After the adsorption of fluoride, the atomic binding oxygen peak at 49.96 eV absolutely disappeared, while more Mg—OH atomic binding peaks are formed at 49.43 eV. It is caused by the reaction of magnesium oxide with water to produce $Mg(OH)_2$. Furthermore, the analysis of the Mg 2p orbital after adsorption of fluoride reveals a partial binding energy peak shifting to 50.2 eV, indicating that electronegativity value of fluoride exceeds that associated with both oxygen and hydroxyl. Consequently, it can be seen from the above that the Mg—F peak after adsorption is transformed from the Mg—O peak and Mg—OH peak. It can be inferred that this phenomenon arises from the reciprocal action between fluoride and magnesium ions, leading to a fractional increment in the binding energy of the Mg 2p orbitals. It indicates that Mg^{2+} exerts a significant influence in the adsorption process and interacts with fluoride [35]. Fig. 9(d) shows the O1s spectra

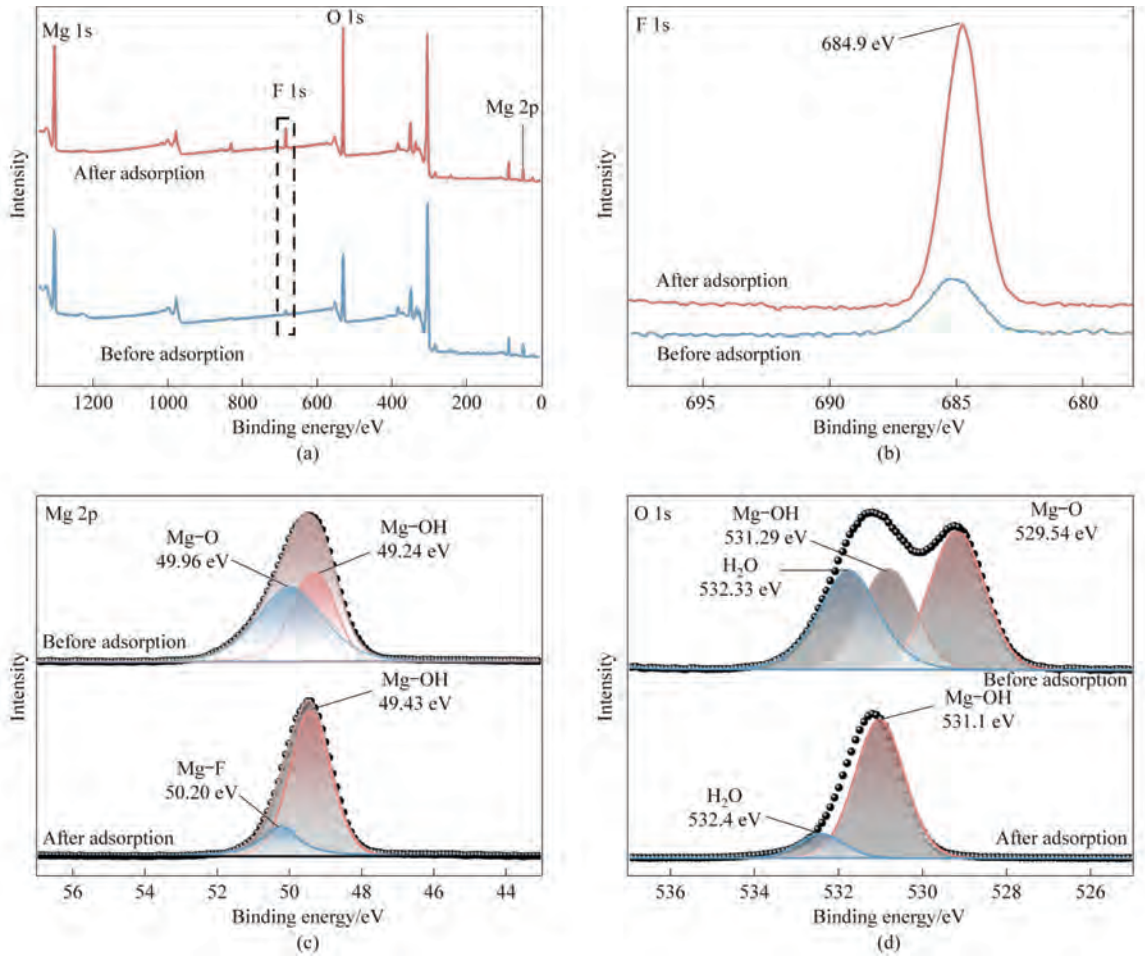

Fig. 9. (a) XPS measurement spectra of MOAS before and after adsorption, (b) XPS F 1s spectra of MOAS before and after adsorption, (c) Mg 2p spectra of MOAS before and after adsorption, and (d) O 1s spectra of MOAS before and after adsorption.

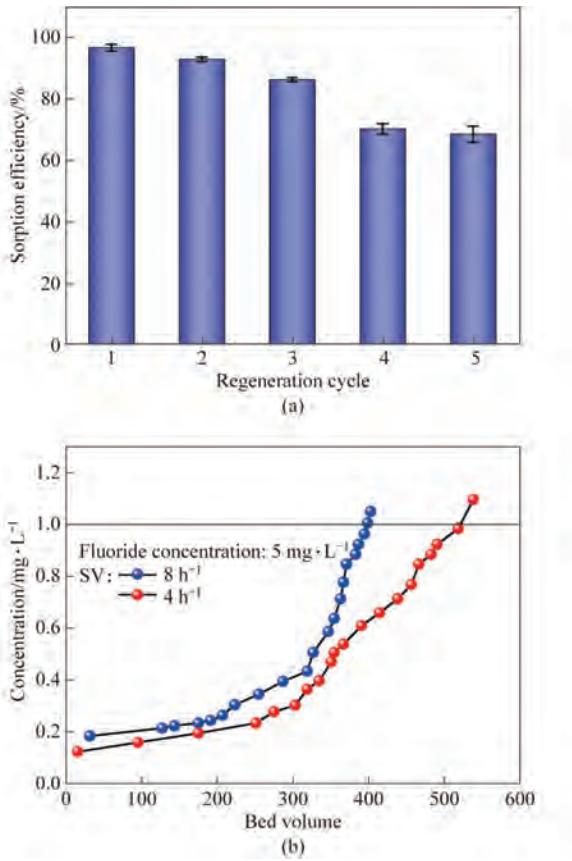

Fig. 10. (a) Removal efficiency of fluoride by MOAS after regeneration cycle, and (b) MOAS penetration curve under different SV.

before and after MOAS adsorption of fluoride, and three peaks can be observed as 529.54 eV, 531.29 eV and 532.33 eV, respectively. The peak at 529.54 eV is ascribed to lattice oxygen atoms bound to magnesium atoms. The peaks at 531.29 eV and 532.33 eV are attributed to the hydroxyl group formed by $Mg(OH)_2$ and adsorbed water, respectively. After adsorption, the peak at 529.54 eV disappeared, and only two peaks of 531.1 eV and 532.4 eV were observed. It is caused by the reaction of oxygen atoms in the lattice were replaced by hydroxyl groups to form Mg—OH [14] and magnesium oxide with water to produce $Mg(OH)_2$, which is accords with the results observed by FTIR.

3.6. Desorption and regeneration

Repeatability is an important part of evaluating the economic benefits of adsorbents. Fig. 10(a) shows the removal efficiency of fluoride by MOAS after adsorption-regeneration cycles. The concentration of fluoride was 10 $mg \cdot L^{-1}$ and the adsorption dose of MOAS was 5 $g \cdot L^{-1}$. The MOAS adsorbed fluoride was desorbed using 50 ml of 1 $mol \cdot L^{-1}$ NaOH and then placed in a shaker, where it was shaken at 250 $r \cdot min^{-1}$ and 25 °C for 24 h. MOAS was subjected to desorption, which was rinsed with deionized water and then heat-treated at 500 °C for 4 h. The removal efficiencies of the first, second, and third adsorption-desorption processes are 96.40%, 92.58%, and 86.01%, respectively. The removal efficiency gradually decreases with the repeated use of MOAS. However, even after 5 cycles, the removal efficiency still reaches a notable level of 68.28%. Following the regeneration process, the active sites of adsorbents decrease and due to partial desorption of fluoride and pore plugging, resulting in a reduction in MOAS effectiveness for removing fluoride [38].

3.7. Adsorption column experiment

In this experiment, MOAS was fixed in a chromatographic column for assessing its adsorption capacity to fluoride-containing wastewater. In the experimental process, a glass chromatographic column whose diameter was 8 mm was employed. The adsorption column had a volume of 5 ml and was 100 mm in height. The influent fluoride concentration was established at 5 $mg \cdot L^{-1}$, whereas the space velocity (SV) was modulated to magnitudes of 4 h^{-1} and 8 h^{-1}, respectively. The water inlet mode employed an up-flow configuration, maintaining a stable temperature of 25 °C. Periodic sampling from the outlet was conducted to determine the concentration of fluoride. The volume of treated wastewater was divided by the volume of the adsorption column to determine the bed volume (BV). Fig. 10(b) shows the penetration curves of fluoride adsorbed by MOAS at different flow rates. Before the treatment of 540 BV and 400 BV, the fluoride concentration extant in the effluent was persistently retained at a level beneath 1 $mg \cdot L^{-1}$, indicating that MOAS has great potential for efficient fluoride removal in practical applications.

3.8. Actual wastewater experiment and cost analysis

In order to investigate the practical application ability of MOAS, the actual wastewater sample test was carried out. The actual wastewater sample was from Changxin Memory Technologies in Hefei, Anhui Province in China. and the initial fluoride concentration was 9.31 $mg \cdot L^{-1}$. As shown in Fig. S6, after 120 min of treatment, the fluoride concentration in the wastewater was finally lower than 1 $mg \cdot L^{-1}$, which meets the national emission standard. At the same time, the cost of MOAS was investigated. As shown in Table S3, the lowest price of synthetic MOAS was 5.8 $USD \cdot g^{-1}$, which was much higher than the price of commercial defluorination adsorbents such as natural boiling stone [39] and biomass [40]. Although the chemical cost of adsorption of MOAS remains high, this work provides a promising basis for continued research into oxides as more economical adsorbents for fluorine pollution.

4. Conclusions

In this work, the loading ratio of magnesium oxide reached 230% for MOAS prepared by hydrothermal method. Adsorption kinetics and adsorption isotherms indicated that the adsorption of fluoride by MOAS is layered adsorption dominated by chemical adsorption, and the adsorption site was the main factor affecting the adsorption. MOAS maintained the high adsorption efficiency of fluoride in a wide pH range and under the various competitive anions, respectively. The adsorption mechanism of MOAS was ascribed to the coordination of fluoride and the exchange with hydroxyl groups. The DFT analysis further demonstrated the MOAS has a stable structure with a binding energy of −14.1 eV. After several desorption-regeneration cycles, MOAS still maintained the adsorption efficiency of 68.28%. The experiments conducted on the adsorption column revealed that MOAS holds the potential for practical applications.

CRediT Authorship Contribution Statement

Chenxin Ding: Writing — original draft, Methodology, Investigation, Formal analysis, Data curation. Zhen Jin: Writing — review & editing, Supervision, Project administration, Funding acquisition,

Conceptualization. Qianxi Li: Validation, Formal analysis. Shuhao Zhou: Validation, Software. Yuru Sun: Visualization, Resources, Formal analysis.

Declaration of Competing Interest

The authors declare that they have no known competing financial interests or personal relationships that could have appeared to influence the work reported in this paper.

Acknowledgements

This work was supported in part by Natural Science Foundation of Anhui Province (2008085MB44), Natural Science Research Project of Anhui Educational Committee (2022AH040046, 2024AH050247), Excellent Scientific Research and Innovation Team in Colleges and Universities of Anhui Province (2022AH010017), Open Project of State Key Laboratory (SKLECRA20230FP01).

Supplementary Material

Supplementary data to this article can be found online at https://doi.org/10.1016/j.cjche.2025.05.030.

References

[1] V. Ganvir, K. Das, Removal of fluoride from drinking water using aluminum hydroxide coated rice husk ash, *J. Hazard. Mater.* 185 (2–3) (2011) 1287–1294.
[2] A. Rathnayake, O. Hettithanthri, S. Sandanayake, K. Mahatantila, A.U. Rajapaksha, M. Vithanage, Essence of hydroxyapatite in defluoridation of drinking water: a review, *Environ. Pollut.* 311 (2022) 119882.
[3] J. Vijayeeswarri, M. Geethapriyai, V. Ramamurthy, Community level defluoridation of groundwater with limestone derived adsorbent, *Process, Saf. Environ. Prot.* 127 (2019) 9–15.
[4] M. Wang, X.L. Yu, C.L. Yang, X.Q. Yang, M.Y. Lin, L.T. Guan, M.F. Ge, Removal of fluoride from aqueous solution by Mg-Al-Zr triple-metal composite, *Chem. Eng. J.* 322 (2017) 246–253.
[5] C.F.Z. Lacson, M.C. Lu, Y.H. Huang, Fluoride-rich wastewater treatment by ballast-assisted precipitation with the selection of precipitants and discarded or recovered materials as ballast, *J. Environ. Chem. Eng.* 9 (4) (2021) 105713.
[6] B.S. Rathi, P.S. Kumar, G. Rangasamy, M. Badawi, T.M. Aminabhavi, Membrane-based removal of fluoride from groundwater, *Chem. Eng. J.* 488 (2024) 150880.
[7] F. Djouadi Belkada, O. Kitous, N. Drouiche, S. Aoudj, O. Bouchelaghem, N. Abdi, H. Grib, N. Mameri, Electrodialysis for fluoride and nitrate removal from synthesized photovoltaic industry wastewater, *Sep. Purif. Technol.* 204 (2018) 108–115.
[8] U.S. Rashid, A.N. Bezbaruah, Citric acid modified granular activated carbon for enhanced defluoridation, *Chemosphere* 252 (2020) 126639.
[9] A. Jeyaseelan, A.A. Ghfar, M. Naushad, N. Viswanathan, Design and synthesis of amine functionalized graphene oxide for enhanced fluoride removal, *J. Environ. Chem. Eng.* 9 (4) (2021) 105384.
[10] M. Sadhu, P. Bhattacharya, M. Vithanage, P. Padmaja Sudhakar, Adsorptive removal of fluoride using biochar–A potential application in drinking water treatment, *Sep. Purif. Technol.* 278 (2021) 119106.
[11] O. Uzun, Z. Gokalp, H. Ali Irik, I.S. Varol, F.O. Kanarya, Zeolite and pumice-amended mixtures to improve phosphorus removal efficiency of substrate materials from wastewaters, *J. Clean. Prod.* 317 (2021) 128444.
[12] S. Manna, P. Das, P. Basak, A.K. Sharma, V.K. Singh, R.K. Patel, J.K. Pandey, V. Ashokkumar, A. Pugazhendhi, Separation of pollutants from aqueous solution using nanoclay and its nanocomposites: a review, *Chemosphere* 280 (2021) 130961.
[13] G.C. Velazquez-Peña, M.T. Olguín-Gutiérrez, M.J. Solache-Ríos, C. Fall, Significance of FeZr-modified natural zeolite networks on fluoride removal, *J. Fluor. Chem.* 202 (2017) 41–53.
[14] Z. Jin, Y. Jia, K.S. Zhang, L.T. Kong, B. Sun, W. Shen, F.L. Meng, J.H. Liu, Effective removal of fluoride by porous MgO nanoplates and its adsorption mechanism, *J. Alloys Compd.* 675 (2016) 292–300.
[15] S.K. Sahoo, G.K. Panigrahi, J.P. Dhal, J.K. Sahoo, A.K. Behera, P.C. Panda, P. Patel, S.K. Mund, S.M. Muduli, L. Panda, Co-axial electrospun hollow MgO nanofibers for efficient removal of fluoride ions from water, *Colloids Surf. A Physicochem, Eng. Aspects* 652 (2022) 129877.
[16] Z. Jin, Y. Jia, T. Luo, L.T. Kong, B. Sun, W. Shen, F.L. Meng, J.H. Liu, Efficient removal of fluoride by hierarchical MgO microspheres: performance and mechanism study, *Appl. Surf. Sci.* 357 (2015) 1080–1088.
[17] A.Y. Li, W.Z. Ge, L.H. Liu, G.H. Qiu, Preparation, adsorption performance and mechanism of MgO-loaded biochar in wastewater treatment: a review, *Environ. Res.* 212 (Pt B) (2022) 113341.
[18] X.N. Liu, J.Y. Fu, Y.W. Tang, R.L. Smith Jr., X.H. Qi, Mg-coordinated self-assembly of MgO-doped ordered mesoporous carbons for selective recovery of phosphorus from aqueous solutions, *Chem. Eng. J.* 406 (2021) 126748.
[19] A. Nagaraj, D. Govindaraj, M. Rajan, Magnesium oxide entrapped polypyrrole hybrid nanocomposite as an efficient selective scavenger for fluoride ion in drinking water, *Emergent Mater* 1 (1) (2018) 25–33.
[20] C. Sairam Sundaram, N. Viswanathan, S. Meenakshi, Defluoridation of water using magnesia/chitosan composite, *J. Hazard. Mater.* 163 (2–3) (2009) 618–624.
[21] B.W. Liu, L. Ai, M. Lei, H.F. Lin, Efficient fluoride removal using nano MgO: mechanisms and performance evaluation, *Environ. Sci. Pollut. Res.* 31 (19) (2024) 28428–28442.
[22] Y.F. Xiao, Y. Zhang, D.C. Wang, Y.M. Su, J. Wu, J.Q. Liu, L.L. Yang, Z. Jin, Hydrothermal synthesis of lanthanum oxide nanoparticles modified pumice: high lanthanum oxide loading ratio and efficiency phosphate removal, *J. Environ. Chem. Eng.* 12 (1) (2024) 111587.
[23] N.A. Oladoja, S. Chen, J.E. Drewes, B. Helmreich, Characterization of granular matrix supported nano magnesium oxide as an adsorbent for defluoridation of groundwater, *Chem. Eng. J.* 281 (2015) 632–643.
[24] C. Gogoi, J. Saikia, S. Sarmah, D. Sinha, R.L. Goswamee, Removal of fluoride from water by locally available sand modified with a coating of iron oxides, *Water Air Soil Pollut.* 229 (4) (2018) 118.
[25] K.H. Chu, M. Ali Hashim, Y.T. da Costa Santos, J. Debord, M. Harel, J.C. Bollinger, The Redlich–Peterson isotherm for aqueous phase adsorption: Pitfalls in data analysis and interpretation, *Chem. Eng. Sci.* 285 (2024) 119573.
[26] S.M. Maliyekkal, S. Shukla, L. Philip, I.M. Nambi, Enhanced fluoride removal from drinking water by magnesia-amended activated alumina granules, *Chem. Eng. J.* 140 (1–3) (2008) 183–192.
[27] P.Y. Zhu, H.Z. Wang, B.W. Sun, P.C. Deng, S.Q. Hou, Y.W. Yu, Adsorption of fluoride from aqueous solution by magnesia-amended silicon dioxide granules, *J. Chem. Technol. Biotechnol.* 84 (10) (2009) 1449–1455.
[28] Q.S. Zhou, B.X. Ren, Y.Q. Wei, S.Q. Tian, X. Jin, F.Z. Jiang, Z.G. Lin, X.J. Yang, Efficient removal of fluoride from water: adsorption performance of MgO-x adsorbents derived from Mg-MOF-74 and insights from DFT calculations, *Sep. Purif. Technol.* 352 (2025) 128190.
[29] H.Y. Zhang, J.D. Hu, J. Xie, S.Q. Wang, Y.L. Cao, A solid-state chemical method for synthesizing MgO nanoparticles with superior adsorption properties, *RSC Adv.* 9 (4) (2019) 2011–2017.
[30] C.M. Su, J. Zhang, First-principles study on growth mechanism of TiN on MgO (1 0 0) and (1 1 0) surfaces, *Comput. Mater. Sci.* 189 (2021) 110257.
[31] G.C. Lv, S.Z. Li, H. Zhang, W.J. Qian, J. Cheng, P. Qian, CO_2 adsorption on a K-promoted MgO surface: a DFT theoretical study, *Surf. Sci.* 749 (2024) 122575.
[32] M. Dekermenjian, A. Merlen, A. Ruediger, M. Rérat, Water adsorption on MgO surfaces: a vibrational analysis, *Crystals* 13 (8) (2023) 1153.
[33] N.M. Adhikari, P. Zarzycki, Z.M. Wang, K.M. Rosso, pH-dependent reactivity of water at MgO, 100) and MgO(111) surfaces, *Phys. Chem. Chem. Phys.* 27 (8) (2025) 4343–4354.
[34] R.R. Devi, I.M. Umlong, P.K. Raul, B. Das, S. Banerjee, L. Singh, Defluoridation of water using nano-magnesium oxide, *J. Exp. Nanosci.* 9 (5) (2014) 512–524.
[35] W. Guo, H.F. Lin, H.X. Zhu, M. Lei, J.P. Feng, Preparation and application of magnesium oxide nanoparticles for superiorly fluoride removal, *J. Alloys Compd.* 960 (2023) 170935.
[36] D.A. Nguyen, V.B. Nguyen, A. Jang, Integrated adsorption using ultrahigh-porosity magnesium oxide with multi-output predictive deep belief networks: a robust approach for fluoride treatment, *Chem. Eng. J.* 484 (2024) 149586.
[37] J.T. Newberg, D.E. Starr, S. Yamamoto, S. Kaya, T. Kendelewicz, E.R. Mysak, S. Porsgaard, M.B. Salmeron, G.E. Brown, A. Nilsson, H. Bluhm, Formation of hydroxyl and water layers on MgO films studied with ambient pressure XPS, *Surf. Sci.* 605 (1–2) (2011) 89–94.
[38] X. Borgohain, A. Boruah, G.K. Sarma, M.H. Rashid, Rapid and extremely high adsorption performance of porous MgO nanostructures for fluoride removal from water, *J. Mol. Liq.* 305 (2020) 112799.
[39] S. De Gisi, G. Lofrano, M. Grassi, M. Notarnicola, Characteristics and adsorption capacities of low-cost sorbents for wastewater treatment: a review, *Sustain. Mater. Technol.* 9 (2016) 10–40.
[40] S. Praveen, R. Gokulan, T.B. Pushpa, J. Jegan, Techno-economic feasibility of biochar as biosorbent for basic dye sequestration, *J. Indian Chem. Soc.* 98 (8) (2021) 100107.
[41] K.S. Zhang, S.B. Wu, J.Y. He, L. Chen, X.G. Cai, K. Chen, Y.L. Li, B. Sun, D.Y. Lin, G. Q. Liu, L.T. Kong, J.H. Liu, Development of a nanosphere adsorbent for the removal of fluoride from water, *J. Colloid Interface Sci.* 475 (2016) 17–25.
[42] J. Xu, J. Gao, M.M. Wang, S. Tian, C.X. Lin, Y.G. Xia, Synthesis of a Ce–La adsorbent with large adsorption capacity for efficient fluoride removal from leaching solution of spent lithium-ion batteries, *Energy Fuels* 38 (8) (2024) 7379–7388.
[43] P.H. Chen, W.B. Zhang, M.L. Li, P. Ai, L. Tian, H.L. Jiang, Facile synthesis of magnetic La–Zr composite as high effective adsorbent for fluoride removal, *RSC Adv.* 6 (42) (2016) 35859–35867.
[44] W. Guo, H.F. Lin, H.X. Zhu, W. Mo, X.J. Su, J.L. Yang, S.J. Ma, J.P. Feng, M. Lei, Efficient removal of fluorine by carbon fiber supported Mg-Fe binary metal oxide composite adsorbent and mechanism analysis based on DFT, *Sep. Purif. Technol.* 330 (2024) 125320.

[45] Y. Zhang, G.S. Xu, M.D. Xu, D.C. Wang, H. Wang, Y. Zhan, Z. Jin, Preparation of MgO porous nanoplates modified pumice and its adsorption performance on fluoride removal, *J. Alloys Compd.* 884 (2021) 160953.
[46] F. Li, Y.T. Zhang, B. Xu, Y.Q. Liu, H.Y. Qiu, G.H. Lan, Q.X. Xu, Synthesizing a novel Zr/Fe/Al-incorporated cross-linked chitosan as absorbent for effective removal of fluoride from aqueous solution, *Water Air Soil Pollut.* 232 (10) (2021) 401.
[47] Y.X. Zhang, Y. Jia, Preparation of porous alumina hollow spheres as an adsorbent for fluoride removal from water with low aluminum residual, *Ceram. Int.* 42 (15) (2016) 17472–17481.
[48] C. Zhang, Y.Z. Li, T.J. Wang, Y.P. Jiang, J. Fok, Synthesis and properties of a high-capacity iron oxide adsorbent for fluoride removal from drinking water, *Appl. Surf. Sci.* 425 (2017) 272–281.